Nanoscale

PAPER

View Article Online
View Journal | View Issue

Cite this: *Nanoscale*, 2026, **18**, 3658

Pulsed-laser induced gold microparticle fragmentation by thermal strain

Yogesh Pokhrel,[a] Meike Tack,[b] Sven Reichenberger,[b] Matteo Levantino[c] and Anton Plech*[a]

Laser fragmentation of suspended microparticles (MP-LFL) is an upcoming alternative to laser ablation in liquid (LAL) that allows the delivery processes to be streamlined and the irradiation conditions to be optimized for superior efficiency. However, the structural basis of this process is not well understood to date. Herein, we employed ultrafast X-ray scattering upon picosecond laser excitation of a gold microparticle suspension in order to understand the thermal kinetics as well as structure evolution after fragmentation. The experiments are complemented by simulations according to the two-temperature model to verify the spatiotemporal temperature distribution. It is found that above a fluence threshold of 750 J m^{-2} the microparticles are fragmented within a nanosecond into several large pieces where the driving force is the strain due to strongly inhomogeneous heat distribution on the one hand and stress confinement due to ultrafast heating compared to stress propagation on the other hand. In addition, limited formation of small clusters is attributed to photothermal decomposition on the front side of the microparticles at a fluence of 2700 J m^{-2}.

Received 16th October 2025,
Accepted 2nd January 2026

DOI: 10.1039/d5nr04365d

rsc.li/nanoscale

1 Introduction

Laser synthesis of nanoparticles in liquids has attracted much attention within the past years because of the prospect of producing a wide variety of particle materials not only in small on-demand batch processes but also in gram-scale synthesis under semi- or even fully continuous flow conditions.[1,2] At the same time, several obstacles have to be overcome to define the product particles by size, chemical speciation, and yield of the process. The primary approach is to place a bulk target in a liquid and irradiate it by short-pulse lasers, coined laser ablation in liquid (LAL).[3] Size definition and speciation in LAL is limited due to the number of competing fundamental processes, including evaporation,[4] spallation, thermomechanical disruption,[5] near-field effects,[6] bubble formation, or reactions of the solvent with limited ability to replace the materials between laser pulses. LAL typically produces multimodal size distributions, including size increase[7] of the product colloid through repeated laser melting and fusing (LML) and redox reactions with the solvent,[8,9] and by carbon shell formation in organic solvents,[10] respectively.

In order to harvest very small nanoparticles and clusters that show particularly promising catalytic or photonic activity, a second step of laser fragmentation in liquids (LFL) can be added to the process chain. LFL can be designed to operate on liquid jets that replace the colloid in a defined way and allows us to quantify the laser fluence applied more easily[11] by masking compared to that during LAL, which typically exhibits fluence gradients across the laser spot on the flat surface[5] and ongoing erosion of the target[12] with variable efficiency[13] after continuous irradiation. Nanoparticle fragmentation has become much better understood recently due to the combined impact of large-scale simulations and experimental efforts to resolve the spatiotemporal evolution of colloidal structures down to atomic length scales.[14–16] Complete fragmentation of initially formed colloidal particles tens of nanometers in size can be achieved with picosecond pulses when the applied laser fluence exceeds 9–12 times the lattice melting threshold fluence, yet remains below the energy needed for full evaporation.[16] The underlying mechanism is based on (thermal) phase explosion and spinodal decomposition. Single-particle studies have also revealed that a thermomechanical effect may play a role in the fragmentation of gold nanoparticles when the employed laser pulse duration (and hence the related, characteristic particle heating time) remains below the characteristic phonon propagation time (proportional to the speed of sound within the fragmented material). In such cases, the

[a]*Institute for Photon Science and Synchrotron Radiation, Karlsruhe Institute of Technology, Hermann-von-Helmholtz-Platz 1, D-76344 Eggenstein-Leopoldshafen, Germany. E-mail: anton.plech@kit.edu*
[b]*Department of Technical Chemistry I and Center for Nanointegration Duisburg-Essen, University of Duisburg-Essen, Universitätsstrasse 7, D-45141 Essen, Germany*
[c]*European Synchrotron Radiation Facility, 71, avenue des Martyrs, CS 40220, F-38043 Grenoble, France*

stress confinement criterion is fulfilled and fragmentation proceeds photomechanically, as observed through void formation in the particle center.[14,17] Both the experimental investigation and theoretical description of nanoparticle colloids are conceptually simplified because energy deposition and flow within the particles typically occur on time scales much shorter than structural transformations such as melting or decomposition.

Recently, several groups have followed the approach of MP-LFL by using commercially available microparticles as feedstock to produce the desired small nanoparticles.[18–22] This approach has been shown to robustly yield nanoparticles smaller than 3 nm, to allow for single-step laser processing, but also to control the surface oxidation of the produced nanoparticles, when applying greater numbers of laser pulses. The ability to process material in a continuous jet[23] is important for defining the required mass-specific energy input and overall efficiency of productivity, which can match or even surpass that of LAL.[2,24]

While laser irradiation of microparticles in a liquid may be viewed as a variant of LFL, in some respects it shares processes that are found in LAL, such as inhomogeneous irradiation of the microparticle surface and tentative competition of processes pertinent to fragmentation as well as ablation.

Paltauf and Schmidt-Kloiber[25] have previously set the scene for microparticle irradiation in liquids by optical stroboscopy. They describe liquid cavitation and stress confinement inside spheres of sub-millimeter sizes that lead to spallation by photoacoustic stress from the center of the particles. Spherical particles accumulate higher stress amplitude due to their high symmetry as compared to cylindrical or irregularly formed particles. Kuzmin *et al.*[26] have described the fragmentation of microscale aluminum particles by combined action of fission ("bisection") of the overexcited molten particles and thermal detachment of very small clusters. Sattari *et al.*[27] irradiated oxide microparticles in a gas stream and found an increased yield of nanoparticles below a size threshold of 100 nm with increased laser fluence. Spellauge *et al.*[20] have recently combined visualization of single-microparticle fragmentation with quantification of product size distributions. Deducing the stress amplitudes from observations of shock-wave and cavitation-bubble velocities allowed us to assess both the energy efficiency of the process and the transient state of irradiated IrO_2 microparticles. In summary, irradiating microparticles with short laser pulses in the strain-confinement regime is expected to generate a spatially inhomogeneous excitation profile across each microparticle, accompanied by important strain waves and a more complex fragmentation process than that of nanoparticles with homogeneous excitation density.[16] Elastic properties of the microparticles, such as brittleness, are therefore anticipated to play a more important role.[2]

To investigate these effects, we performed picosecond-resolved pump–probe experiments on size-defined gold microparticles in a water jet by using pulsed X-rays as a structural probe. The resulting X-ray scattering allows us to resolve the thermal and melting dynamics of the particles with high temporal precision and directly observe the fragmentation process. By generating the heat flow using numerical simulations according to the two-temperature model of electronic and phonon subsystems of the particles, the time scales for heat flow and particle melting are revealed. The close agreement between experimental and theoretical fluences shows that fragmentation is driven by strain gradients across the particles. In the low-fluence regime investigated here, fission into particles of tens to hundreds of nanometers dominates, whereas fragmentation into nanometer-sized clusters plays a minor role and will emerge only at higher fluence.

2 Experimental details and analysis

2.1 Microparticle irradiation

The gold microparticle powder with quasi-spherical particles and a narrow size distribution close to 1.2 μm in diameter (Evochem, Offenbach, Germany) was suspended in water by ultrasonic agitation. Scanning electron microscopy (SEM) images of the powder are displayed in Fig. 1a. The colloid was irradiated from the side in a free round jet by 1 ps laser pulses at 400 nm from a regenerative-amplifier laser system (Coherent) at beamline ID09[28] of the European Synchrotron

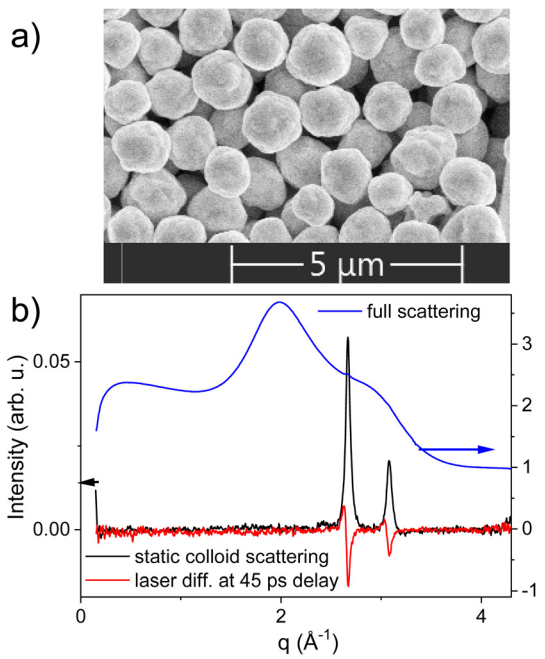

Fig. 1 (a) Scanning electron microscopy image of a powder of quasi-spherical gold microparticles. (b) X-ray scattering distribution of an aqueous colloid containing 400 mg L^{-1} gold microparticles with full scattering including the water phase in blue, the extracted static scattering from the gold particles after subtracting pure water in black, mainly showing the (111) and (200) gold powder peaks at 2.67 and 3.1 $Å^{-1}$, respectively. Upon laser excitation the powder peaks shift transiently and eventually are reduced in intensity as marked by the difference scattering of the colloid at 45 ps delay relative to a negative delay between laser and X-ray pulses in red, respectively.

Radiation Facility (Grenoble, France). A pulsed X-ray beam was utilized to probe the structure of the sample at the same repetition rate of 1 kHz. The laser fluence was estimated with 20% variation across the probed volume. The liquid was collected after irradiation at an incident fluence of 2700 J m^{-2} and analyzed *via* SEM and transmission electron microscopy (TEM). For this analysis, the fragments are stabilized by 0.5 M NaOH at pH 10. Note that irradiated particles in the collected liquid are much less abundant than non-irradiated ones because of the difference in laser spot and jet size. Therefore, the size distributions and concentrations found in the TEM analysis are not representative of the *in situ* abundance of fragmentation products.

2.2 Scattering signal

The scattered X-rays are recorded on a 2D area detector (Rayonix HS170), whose distance from the sample can be varied to cover a scattering vector $q = 4{\cdot}\pi/\lambda{\cdot}\sin(2\Theta/2)$ from 0.01 to 5 $Å^{-1}$, with λ and 2Θ being the X-ray wavelength and full scattering angle, respectively. The difference $\Delta I(q)$ of two measurements with either positive or negative delay τ after laser excitation contains only the signal pertaining to laser-induced structural changes in the sample with delay τ. The observables deduced from this signal have been discussed in detail earlier[15,16] and explained in the SI. In brief, the gold (111) powder peak can be analyzed in position, amplitude, and width to conclude on particle heating, melting and strain formation. Liquid scattering can provide information on the thermodynamic state of water. The full X-ray scattering intensity $I(q)$ in a q range between 0.2 and 4.3 $Å^{-1}$ is shown in Fig. 1 (b) together with the contribution from gold powder scattering, as well as a difference scattering curve at a delay of 45 ps and fluence of 2700 J m^{-2}. Small-angle scattering finally reflects all changes in the large-scale structure from a few nm to about 60 nm in the present case. Previously, we have derived changes of particle sizes and shapes of irradiated initial nanoparticles[16,29] as well as the quantification of the formation of vapor bubbles by cavitation.[30,31]

However, the q values that indicate shape changes for the microparticles (Guinier range close to $q_{\mathrm{Guinier}} \simeq \pi/R$ with R being the characteristic length scale or the radius) were below the accessible detection range of the standard pinhole detector setup used in this study (lower limit 0.009 $Å^{-1}$, which practically allows one to resolve particles of <50 nm in diameter). Small-angle scattering for compact particles generally decays with a power law (Porod law) of $S(q) \propto Kq^{-4}$ for q values larger than the Guinier range independent of the actual radius and can therefore be detected in the accessible q window. The proportionality K can be used to express the total specific surface area A:[32,33]

$$A = \frac{K}{2\pi {r_e}^2 \left(N_A \cdot Z / \left(M \cdot \Delta\rho_{p-l} \right) \right)} \quad (1)$$

with the scattering cross-section expressed by the classical electron radius r_e, Avogadro's constant N_A, atomic number Z, molecular mass M and electron density contrast $\Delta\rho_{p-l}$ between particle p and liquid l. Thus, the amplitude of the SAXS signal is proportional to the total surface area of the particles. The derivation of the amplitude is conveniently performed by averaging the experimental SAXS signal over a finite q range q_P that obeys the Porod law. We chose the interval between 0.014 and 0.056 $Å^{-1}$ to extract $\Delta I(q_P)$.

2.3 Heat flow in the microparticles

Laser excitation and heat flow through the microparticles is simulated by using a numerical code for evaluating laser penetration, coupling of the photons to electrons and phonons (two-temperature model, TTM) and diffusional transport of hot electrons and phonons through the particle. The Python code NTMPy[34] is used by dividing a sphere of 0.6 μm radius into 12 equal annular regions of fixed incidence angle and thickness and combining the slices later (see SI). This approach is limited by neglecting polarization effects and Mie scattering and not allowing for transverse heat transfer (perpendicular to the annual slices). On the other hand, the transport of both electrons and phonons in the slices is correctly described, which matters for gold with a particularly long electron–phonon time and important electron transport.[35,36] The assembly of these independently simulated slices produces the spatiotemporal distribution of heat in a photoexcited gold sphere, as shown in Fig. 2. For visual support, these 12 slices have been interpolated to 36 raster lines in the y dimension.

Threshold temperature changes are defined in a quasistatic model.[4,37] In order to reach the melting point of gold (1336 K) under laboratory conditions, a temperature rise of 1040 K is needed, which can be done by providing energy from a defined fluence value. In order to completely melt the par-

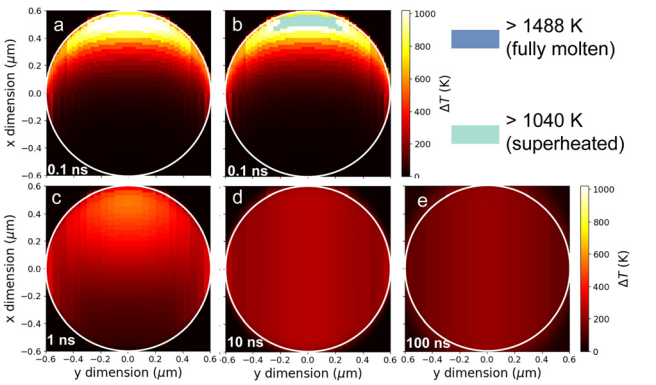

Fig. 2 Numerical simulation (cross-section through the center) of the heat transfer within a single gold microparticle irradiated from the top at a simulated fluence of 85 J m^{-2}. The temperature is color-coded, reaches a rise of 1170 K within 100 ps in the surface layer facing the laser footprint (a). Full melting is assumed when the temperature rise exceeds 1488 K (see text), and a superheated or partially molten state is assigned when the temperature rise exceeds 1040 K, corresponding to the melting point of bulk gold (b). The panels (c)–(e) show the subsequent heat flow through the particle and its cooling at delays of 1 ns, 10 ns and 100 ns, respectively.

ticles, the latent heat has to be provided in addition. With 29.09 kJ mol^{-1} of energy to reach the melting point and a latent heat of 12.55 kJ mol^{-1} (ref. 37) for gold the fluence has to be increased by 43% above the value for reaching the melting point. In order to find the location of complete melting in the simulations, a value of 448 K above the melting point is searched for in the temperature distribution to ensure sufficient energy to overcome the latent heat. Thus, a temperature rise in the simulations of 1488 K has to be obtained to achieve complete melting calorically, although in reality the temperature would not rise above the melting point before full melting is achieved.

3 Results and discussion

3.1 Thermal kinetics

If the excitation depth is smaller than the particle size and heat diffusion proceeds over a slower time scale than electron–phonon coupling or melting/freezing kinetics, the heat distribution in a laser-excited microparticle is not trivial. Fig. 2 shows a cross-sectional heat map through a microparticle at several time delays after laser excitation by a Gaussian pulse of 1 ps duration. At 100 ps (part a) the lattice heating is localized in a surface region of about 200 nm facing the laser direction (from the top). Already, the thickness of this heat-affected zone amounts to more than the laser penetration depth of about 30 nm at 400 nm in the simulation.[36,38] This is a result of the onset of phonon diffusion (lattice heat conduction), but is also caused by transport of heat by the excited conduction electrons prior to coupling to the lattice. One indication of heat transport by hot electrons is the delayed equilibration of electron and phonon temperature with depth, as seen in Fig. S4 of the SI. This is not a result of reduced electron–phonon coupling but of the spreading of hot electrons at a rate faster than phonons.

At the chosen laser fluence one finds that the temperature at the front part of the microparticle has already reached a temperature rise of 1170 K and exceeded the 1040 K increase required to reach the melting point, while it stays below the temperature of 1488 K. Consequently, this region is marked in (b) as superheated, as melting of the whole region would require the additional latent heat to convert into a liquid, which is not provided in full. Local melting may still happen.

At 1 ns delay (c) the heat has penetrated further into the particle, while the fully molten region has become shrunken because of the diffusional transport. At 10 and 100 ns (d and e) heat has spread throughout the particle and eventually will enter the surrounding water, leading to cooling of the particle.

Hereby, the simulated temperatures from Fig. 2 were used to calculate an average particle expansion equivalent to the results of the diffraction experiment shown in Fig. 3. For the experiment, the particle expansion was determined from the average peak shift of the (111) powder peak at given fluence and delay values, taking into account the lattice expansion coefficient α of 14.2 × 10^{-6} K^{-1} at room temperature.[39] The

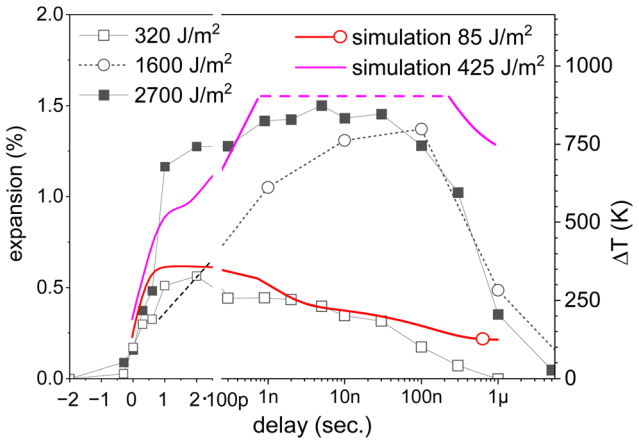

Fig. 3 Time-resolved lattice expansion at several incident laser fluences of 320, 1600 and 2700 J m^{-2} together with simulations of the temperature rise ΔT at corresponding fluences of 85 and 425 J m^{-2} taking into account only parts of the microparticle volume showing a temperature increase of below 1040 K. Along the simulated curve at 425 J m^{-2} the volume fraction below a rise of 1488 K is too small for reliable averaging between 800 ps and 200 ns, and it is thus marked by a dashed line at the maximum observable crystal temperature.

data are overlaid in Fig. 3 at an experimental fluence of 320 J m^{-2}, where particle melting is not yet observed, and for higher fluences of 1600 and 2700 J m^{-2}, plotted as a function of delay (as represented by symbols). The average temperatures at two simulated fluences of 85 and 425 J m^{-2} (spatial temperature maps shown in Fig. 2and 4a–c) are overlaid as full lines. At 320 J m^{-2} the expansion within the recorded time delay remains at around 0.5%, which translates into a temperature change of 300 K or less. The temperature increases rapidly within 200 ps before reaching a plateau and decaying over a 100 ns time scale. This behavior is also reproduced by the simulation and, unlike the volume-averaged experimental result, further allows the interpretation of front-side heating, subsequent spreading of the heat throughout the particles,

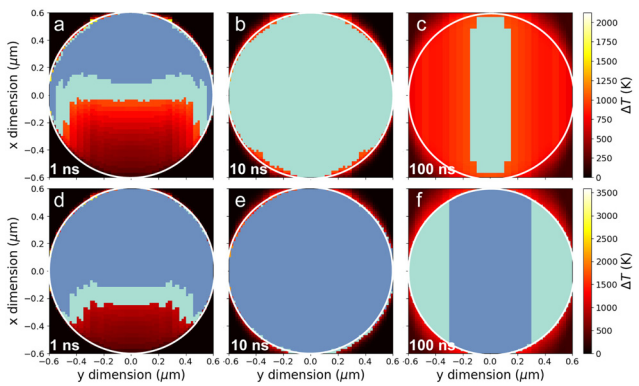

Fig. 4 Numerical simulation of the melting state of a single gold microparticle as a function of delay at a laser fluence of 425 J m^{-2} (a–c) and 717 J m^{-2} (d–f) with the color coding from Fig. 2 marking fully molten regions in blue and superheated regions in light blue.

and the final cooling into the water medium. At 1600 J m^{-2}, the observed experimental behavior differs substantially from the low-fluence excitation, as the temperature rise starts in the same way, but proceeds on a much longer delay to reach the maximum temperature only between 10 and 100 ns.

A quantitative comparison shows that the simulation can reproduce the experimental behavior at 320 J m^{-2} by a calculated fluence of 85 J m^{-2}, which matches the change well in a delay region of 1–10 ns, where the heat is expected to have spread across the particle. The experimental and simulation fluence values differ by a factor of 4. This is still satisfactory considering that the simulation model neglects polarization and also does not incorporate plasmonic effects that may redistribute energy along the particle surface or changes of optical properties with rising electron temperature.[16] According to Mie theory,[40] the scattering of a 1.2 μm gold particle in water amounts to 66% of the total extinction, which is not transformed into heat and thus explains a large part of the difference between experiment and simulation. The corresponding extinction is displayed in the SI, Fig. S2. Matching the lattice expansion in the 1–10 ns region also includes losses from bubble formation at the particle–water interfaces. As displayed in Fig. S5 and S6 of the SI, the water temperature at the particle front can rise by 180 K.

Also, phase transitions such as melting or fragmentation or bubble formation are not included, which consume energy. Indeed, the temperature distribution in the simulated maps shown in Fig. 4 reveals that at 1 ns a large part of the front is molten and heated to much higher temperature. The melting kinetics may have to be included, but it is generally acknowledged that melting at high excitation proceeds within tens of picoseconds, while melting could be delayed to 100–200 ps for homogeneous melting of single-crystal materials.[41,42] Over a longer time scale, we would expect melting to instantly follow the temperature change. Between a temperature increase of 1040 K and 1488 K we marked the respective area as superheated, which may include partial melting. At later delays, the energy spreads across the entire particle, leading to partial or complete melting at 100 ns. A small discrepancy between calculated absorptance and measured energy uptake has been seen previously[16,20,43] and could also be attributed to different loss mechanisms, such as nonlinear optical properties, thermal or acoustic coupling to the medium or laser shielding.

In contrast, at 1600 J m^{-2}, the lattice expansion apparently proceeds more slowly than that at 320 J m^{-2} and reaches maximum expansion only at 10–100 ns. The reason is not modified thermal kinetics at this fluence, but the onset of melting on the picosecond time scale at the particle front. In this case, the molten volume fraction does not contribute to the powder scattering signal, but only the cold (and crystalline) back side. Therefore, the observed lattice temperature is much lower than the equivalent of dissipated energy in the microparticle.

After conduction of thermal energy throughout the particle on a 10 ns time scale, the back side heats up as well. Meanwhile, the front side starts to recrystallize and contribute again to the scattering signal. Therefore, the recorded temperature is highest on the nanosecond time scale before the particles cool through heat transfer to the surrounding water. This behavior is also reflected in the simulation at 425 J m^{-2}, where only the part of the particle below 1488 K was used for calculating the average temperature. The observed temperature is seen to remain at about 500 K up to 0.5 ns only to rise to higher values on the nanosecond time scale. Between 800 ps and 200 ns most of the particle is molten, such that the residual solid part is insufficient to allow us to derive a meaningful average. Therefore these data are replaced by dashed lines.

At 2700 J m^{-2} the temperature rise is again rapid, but the resulting expansion remains below 1.8%, which marks the maximum expansion at the melting point. However, inspecting not only the peak shift, but also the peak intensity (Fig. 5), one recognizes that at 2700 J m^{-2} the particles are molten to a large degree with the remaining crystalline volume residing close to the melting point. Consequently, the measured temperature in the scattering experiment reflects only the still-solid particles, and the observed expansion must remain below the melting-point expansion of 1.8%.

In an alternative approach to the analysis, the (111) powder reflection can be viewed as a superposition of several narrow peaks that result from different parts inside the particle with varying increases of temperature and thus shifted peak positions. The powder profiles extracted at an experimental fluence of 2700 J m^{-2} are shown in Fig. 5(a) for a sequence of time delays. While the non-excited peak (at a delay of 200 ps) is found close to 2.675 $Å^{-1}$, the peaks after excitation shift in position to lower q values, indicating lattice expansion. Additionally, the peak shapes change considerably because of possible melting (loss of peak intensity) and a spatially inhomogeneous temperature profile, as revealed by the simulations. For quantitative analysis, the complete peak shape has been fitted by a superposition of six Gaussian peaks with fixed width but variable position and amplitude. The position of each is converted into a temperature rise by using the thermal expansion coefficient (see above), and the amplitude contributes to the weight factor of each temperature. In this approach, the peak shift is entirely interpreted as local thermal expansion, but not as elastic strain. The latter would show both expansive and compressive contributions, but would be averaged out, when not in synchrony in all particles in the ensemble. In order to reduce bias by the fit limits and starting values, we varied both for different fit runs (using Python code) and averaged over the results to convert the results into a histogram of temperature distribution within the particles. The implicit notion here is that a possible dispersion of excitation across the whole microparticle ensemble is neglected in favor of explaining the change of the powder profile in Fig. 5 (a) as a result of a distribution in temperature in a single particle.

The color map of the temperature-increase probability distribution as a function of delay is shown in Fig. 5(b). At negative delays, the center of probability lies at zero temperature

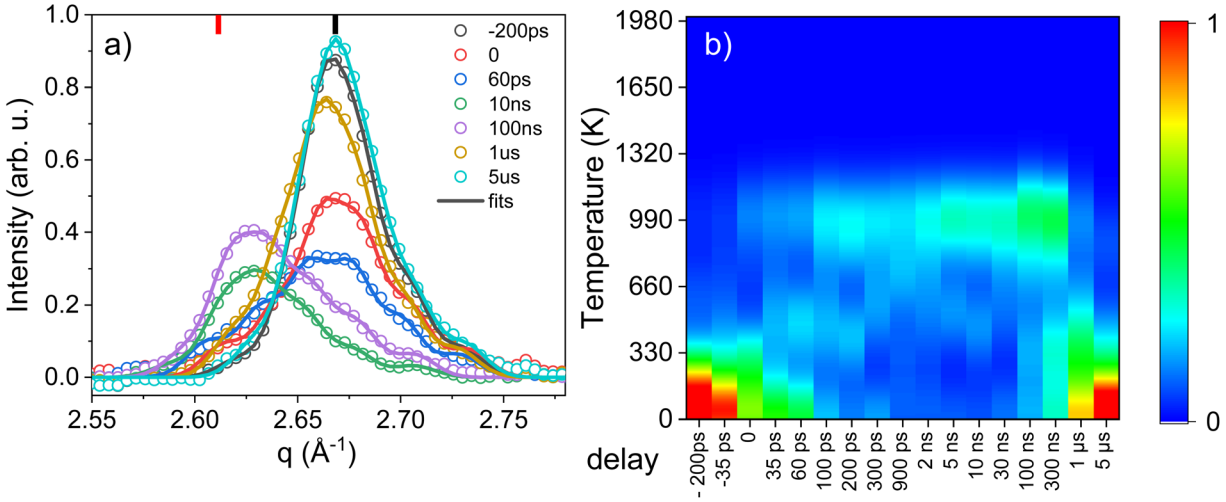

Fig. 5 (a) Powder profiles of the (111) reflection of gold as a function of delay at 2700 J m^{-2}. The lines are fits with the sum of the Gaussian peaks. The vertical bars mark the position of the cold (111) peak (black) and the position of maximum expansion at the melting point. (b) False color map of the extracted temperature-increase probability distribution as a function of delay. The color scale maps the spectral weight of each temperature bin (see the text for details).

change, as expected, but it shifts rapidly to values between 0 and 1040 K with a broad distribution once the excitation arrives.

Later, on a time scale of several nanoseconds, the distribution narrows to a value close to the melting point at ≈1040 K. We interpret this observation in accordance with the simulation results where the temperature was also found to equilibrate throughout the whole microparticle (heat conduction) on the time scale of several nanoseconds. The spread in temperature on the picosecond time scale shows a large difference in temperature to the back part, which is reflected in an increased probability for a range of temperature changes. The temperature spread is subsequently reduced to show a more uniform distribution. Together with the fact that the powder intensity is reduced at the picosecond delays and recovers later, we conclude that the front part may have undergone partial melting and recrystallized when the heat spreads out. In this case, it is natural that, after release of latent heat, the temperature first equilibrates close to the melting point before the particle cools down *via* heat transfer to water. At the latest observed delay the temperature again settles at zero temperature change, indicating a recovery of the crystal lattice. One should add that the experiment is limited in resolving lattice defects or changes in crystalline particle size because of the limited resolution of the experimental setup.

3.2 Particle fragmentation

Thus, both the simulation and the time-resolved scattering show that a microparticle irradiated by a picosecond pulse is heated at the front side with a penetration depth of about 200 nm within the first 200 ps. The energy can cause the front side to melt and dissipate the heat across the whole particle within 10 ns. The release of latent heat from the molten front side after recrystallization adds to the heating of the back side. The cooling *via* heat transfer to the water medium takes place within a time scale of 100 ns–1 µs and is potentially delayed at high fluence due to bubble formation and thermal shielding. The strong temperature gradient between the front side and back side of the particle at delays of <1 ns leads to considerable stress that can cause thermomechanical fracture and particle fragmentation. However, the temperature at the front side can be high enough to cause phase explosion in gold when reaching the spinodal, which is the point of barrierless decomposition into atoms and clusters. With a typical spinodal temperature placed around $0.9T_c$, T_c being the critical temperature of gold, we would expect spinodal decomposition at approximately an energy uptake of 4.4 eV per atom,[16,44] which would be extrapolated to a necessary experimental fluence of 4700 J m^{-2} to reach the spinodal temperature within the front layer of the microparticle.

An additional fragmentation mechanism could be present, which concerns spallation of an excited front layer, which has been observed in laser ablation in liquids.[5,20,45] This is described to take place close to the threshold for laser ablation in air[46] or slightly higher in liquid, which for gold happens at about 22 kJ m^{-2}.[47]

Changes in the scattering signal are detectable not only around the powder peak angles of crystalline gold but also at other scattering vectors. Liquid scattering changes with characteristic functions upon heating and compression/expansion due to slight changes of interatomic distances of water.[16,30,48] The observed changes for microparticle excitation are weak (see Fig. 6) but visible, and indicate bubble formation around the heated particles, caused by the resulting compression of the surrounding bulk water. More prominent changes are seen in the small-angle region, which corresponds to larger length scales and reflects particle-shape changes in general. In the q-range from 0.01 to 0.1 Å^{-1} we observe a drastic increase in

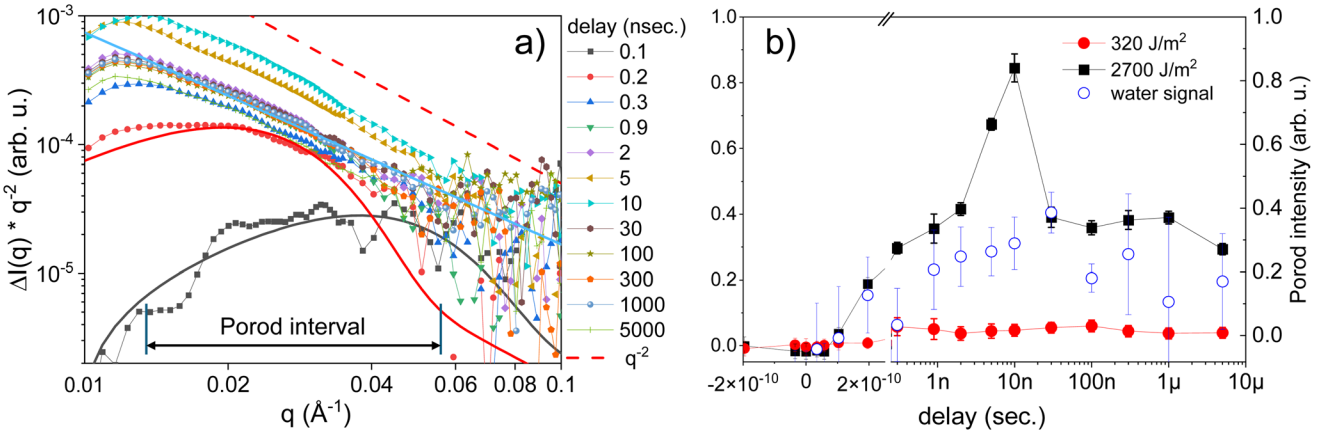

Fig. 6 (a) Kratky representation of the small-angle part of the difference scattering after laser excitation at a fluence of 2700 J m^{-2}. The dashed red line marks a slope of −2 for comparison. The solid lines are fits to the data at delay 0.1 ns (black), 0.2 ns (red) and 1 μs (pale blue) as explained in the text. (b) Change of the integrated (Porod) intensity as a function of delay at 320 J m^{-2} (red bullets) and 2700 J m^{-2} (black squares) together with the amplitude of water difference scattering indicating bubble formation (blue circles) at 2700 J m^{-2}.

scattering, as shown in Fig. 6. At 2700 J m^{-2} the low-q scattering increases as a function of delay. For the earliest delays (100 ps, black curve, and 200 ps, red curve in Fig. 6), the function $\Delta I(q)\cdot q^2$ exhibits a maximum at around 0.035 Å^{-1} and 0.02 Å^{-1}, respectively, while for delays > 200 ps, the shape is monotonic and changes in amplitude, but not in shape. The slope of this signal shows a power law decay of q^{-2}, which clearly indicates that $\Delta I(q)$ scales with q^{-4}, indicative of the Porod region of compact, solid objects. Therefore, it is concluded that the microparticles are being fragmented to form new particles with an increased surface area. As the shape of the curves at these later delays does not change from the power law, it is not possible to derive a size distribution, but one can assume that the formed fragments are still larger than the resolution of the present setup of about 50 nm. At the same time, the increase in surface area according to eqn (1) can be extracted as being proportional to the integrated intensity.

The difference scattering signal at 100 ps and 200 ps has been fitted with fragments of different sizes. The experimental data are best matched when assuming an average particle radius of 12 nm or 23 nm in diameter, respectively. However, these nanoparticles only account for 1% and 2.5% of the total mass. This shows that small particles are emitted from a small volume fraction of the microparticles before the whole particle breaks up. This may be identified with extreme superheating at the front of the microparticles. At later delays (≳300 ps) this signal is still present (as we can observe clusters in the range of 2–20 nm using TEM (see Fig. 7)), but is hidden below the more intense signal from the large fragments. A simulation at a fluence comparable to the experimental fluence of 2700 J m^{-2} results in a temperature increase at the irradiated front of the microparticles of 9700 K, which approaches the spinodal locally.[49] At these later delays, the signal from these first fragments is superseded by the signal from larger fragments as described above.

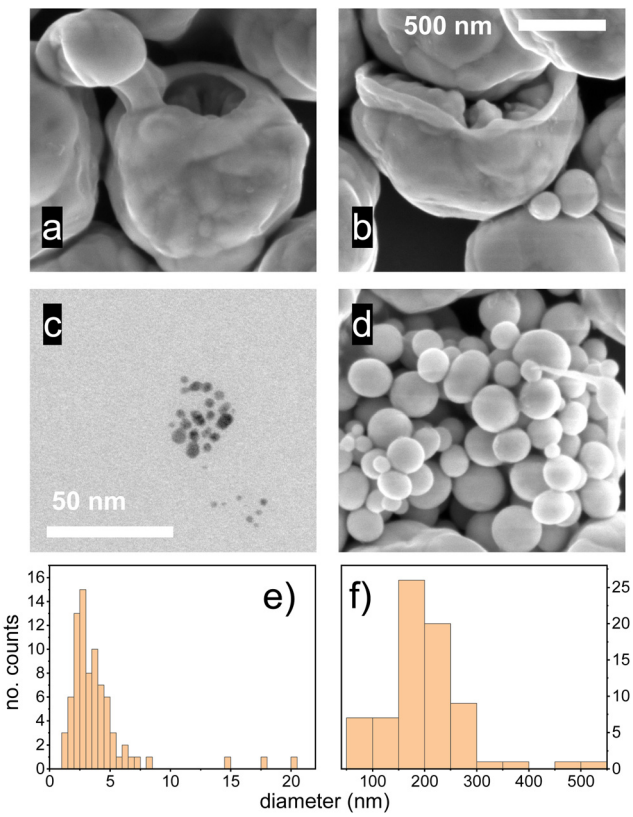

Fig. 7 A set of SEM images of the fragmentation products at the experimental fluence of 2700 J m^{-2} (a, b and d) and a TEM image of the small fragments (c) together with the size histograms of two fragment fractions from 0–25 nm (e) and 75–550 nm (f).

The amplitude of the SAXS signal > 200 ps is converted into an increase in surface area, when an initial microparticle of radius R_0 is fragmented into N smaller fragments of radius R_{frag}. An estimate of the size of the fragments can be given

under the assumption of spherical fragments, assuming that the total mass V_{total} does not change:

$$V_{total} = 4\pi/3 \cdot {R_0}^3 = N \cdot 4\pi/3 \cdot {R_{frag}}^3 \quad (2)$$

Then, the increase in surface area S_{frag}/S_0 can be expressed as:

$$S_{frag}/S_0 = N \cdot {R_{frag}}^2/{R_0}^2 \quad (3)$$

Inserting the criterium of constant particle volume before and after laser fragmentation from eqn (2) into eqn (3) leads to volume normalization and hence yields the ratio of the volume-specific particle surface after ($S_{V,frag}$) and before ($S_{V,0}$) fragmentation:

$$S_{V,frag}/S_{V,0} = R_0/R_{frag} \quad (4)$$

and

$$S_{V,frag}/S_{V,0} = (\Delta I(q_P) + I_0(q_P))/I_0(q_P) \quad (5)$$

using the amplitude of the SAXS signal $\Delta I(q_P)$ and the amplitude of the scattering from the initial microparticles I_0. The latter is derived from a normalization of ΔI by a colloid of known size and concentration (see ref. 16) rather than using the raw scattering.

Following this approach, we estimate that the volume-specific surface of the microparticles has increased by a factor of 10 upon fragmentation at a delay of 1 μs. This would result in a diameter of 80 nm of the presumed spherical products. However, thermomechanical fragmentation of solid particles can lead to nonspherical shapes, which show a higher surface-to-volume ratio, and thus can be larger in size. At two delays of 5 and 10 ns the SAXS intensity is further increased beyond the scattering at 1 μs, which we consider the final state of fragmentation, because of the coincident cooling time. The SAXS signal amplitudes are displayed in Fig. 6(b) at 2700 J m^{-2} and the lower value of 320 J m^{-2}, at which the particles remain in the solid state. At 320 J m^{-2}, barely any difference in the signal is observed, which excludes fragmentation at this fluence. Additionally, the amplitude of the water difference signal is shown (open, blue circles in Fig. 6b) at 2700 J m^{-2}, which starts to rise at 200 ps and does not fully decay within the observed delay range. As we relate this signal to bubble formation, it shows that vapor bubbles around the hot particles are formed and long-lived. Spellauge *et al.*[20] recorded bubbles around individual irradiated IrO_2 particles that have a life time of >10 μs, which agrees well with our findings.

The SAXS signal in Fig. 6(b) shows a rise time >200 ps, which may reflect the finite disintegration speed of a microparticle into spatially separated fragments. The SAXS signal reaches a constant value on the nanosecond scale, indicating a stationary state. This is only interrupted by a signal maximum at 5 and 10 ns as mentioned above. We believe that the nascent bubbles around the particles contribute to the signal at these time delays strongly if their size is only slightly larger than the resolution limit, thus causing a relatively sharp peak in delay.

The more interesting part is the steady-state scattering at 1 μs that represents the final fragment structure after particle cooling. At this fixed delay, the fluence was increased stepwise to track the possible onset of fragmentation. The results are displayed in Fig. 8. As discussed above, the difference-scattering curves exhibit an approximately constant slope in the SAXS region, providing no shape-specific structure to justify applying shape-dependent models for the simulation. The increase in surface area was derived according to eqn (5). The surface area increases in total by a factor of 10 from the initial microparticle surface to that of a number N of fragments, as seen above in the signal intensity change of the time-resolved data. Thus, fragments of about 80 nm in diameter can be formed, which is equivalent to N = 3400 fragments formed. Again, we have no information about the fragment shape, which renders N an approximate number.

The inspection of the SEM and TEM images of the collected colloid reveals partly fragmented microparticles and fragments of variable size (see Fig. 7a–d). A number of the fragments exhibit a large variation in diameter from 75 to 550 nm as seen in Fig. 7d and the histogram in Fig. 7f. Some small fragments can also be found after TEM inspection with particle diameters in the 5 nm range (see TEM image in Fig. 7c and the histogram in Fig. 7e). No statement on relative frequency or fragmentation efficiency can be made from the electron microscopy images, but it is intriguing to discover repeatedly damaged microparticles of apparently initial diameter but featuring an eroded side with a deep indentation. This supports the notion that strain at the irradiated front of the particles

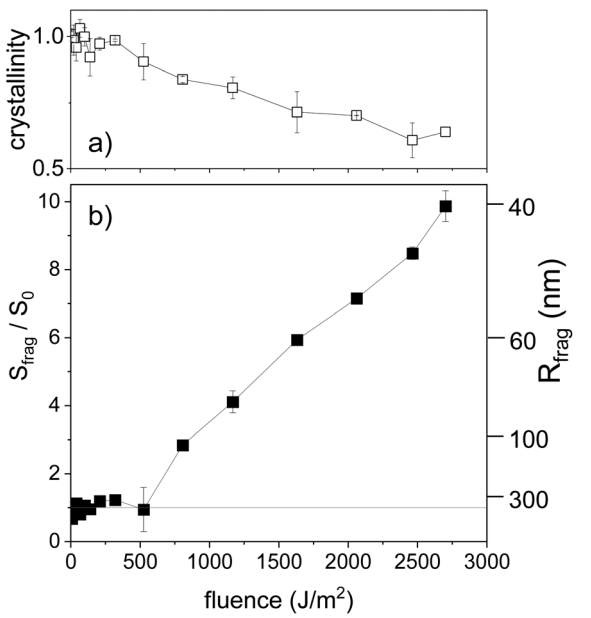

Fig. 8 (a) Solid fraction of microparticle mass at 1–10 ns delay as a function of fluence. (b) Increase in surface area after fragmentation derived from the amplitude of the excess small-angle scattering within the Porod interval as marked in Fig. 6 as a function of fluence. The right-hand axis in (b) indicates the corresponding particle radius, if spherical fragments are assumed.

plays a major role in fragmentation, whereas the back side seems to remain at low temperature and does not show damage. The large fragments, on the other hand, show a compact round shape, which is indicative of at least partial melting. This suggests that the fragmentation mechanism is thermoelastic with thermally induced strain leading to eruption of the front part and emission of partially molten material that forms particles in the 100–500 nm range, which agrees with the SAXS results. Some small fragments in the 5 nm diameter range are formed at the front surface, where the temperature reached a multiple of the melting temperature. Similar observations have been reported by Spellauge *et al.*[24] based on single-particle ultrafast imaging. They reported the dominance of photomechanical fragmentation at low fluence and onset of photothermal (phase explosion) fragmentation at 15 times the photomechanical fragmentation threshold. This mechanism thus shows similarities to laser ablation in liquid, with the heat-affected zone being much smaller than the irradiated target.

The fluence dependence shows that below 500 J m^{-2} no detectable surface area increase is found, which puts the experimental fragmentation threshold at <750 J m^{-2}. At this fluence, we expect the surface temperature on the sub-nanosecond time scale to reach at maximum 2600 K, which raises a volume fraction of 5–10% of the microparticle above the melting-point temperature for some time after laser excitation, while the temperature of the back part of the particle does not differ much from room temperature. At 100 ns, the maximum temperature rise has decayed to 500 K throughout the microparticle. This infers that substantial strain prevails within the microparticle for a delay of up to 1 ns. Note that the acoustic relaxation time τ_{acoust} along the particle diameter D = 1.2 μm is D/v_s with v_s being the speed of sound of gold.[50] Thus, the relaxation time for compression waves is 370 ps, while for shear waves it is 1 ns, which is in good agreement with the previous interpretation. This reveals that at least at the 300 ps time scale, stress is confined in the particle and can cause fragmentation. The crystalline fraction averaged over 1–10 ns as displayed in Fig. 8(a) and reflects the fact that melting occurs to the extent of a variable fraction at the front side, but does not happen across the whole particle. At the highest observed fluence, only about 50% of the particle mass is molten, which could in part also come from an inhomogeneous fluence profile throughout the liquid volume. Starting from the fragmentation threshold at <750 J m^{-2} the surface area increases almost linearly, while the fragment size decreases in an accelerated fashion with fluence.

4. Conclusions

The fragmentation of microparticles by pulsed lasers has become an alternative route to producing defined nanoparticles from a commercially available precursor. It is difficult to resolve the mechanisms of fragmentation by experimental approaches, which leaves conflicting reports on this process in the literature. We used 1 ps, 400 nm laser pulses to photoexcite a colloid of 1.2 μm gold microparticles and monitored their fragmentation using atomically resolving X-ray scattering methods with a time resolution of 60 ps. The powder scattering reveals the temperature dynamics of the microparticles, either as an average over the entire particle or, through detailed analysis of the powder scattering profiles, as a temperature spectrum. At low applied laser fluence, we observe the conventional phenomenon of particles being heated on a 100 ps time scale and subsequently cooling on a 100 ns–1 μs time scale. However, at higher fluence, the response becomes unconventional where the heating seems to be delayed by 1–5 ns relative to the laser impact. This behavior can be understood by calculating the spatiotemporal heat distribution across a spherical particle through full solution of the TTM and the corresponding heat-diffusion equations for this geometry. These simulations reveal that for the first 100–200 ps the particle is only heated at the front side with a penetration depth of 200 nm. This depth results from the combined effects of the optical penetration depth and diffusive energy transport. Despite an electron–phonon coupling of 5–10 ps,[38,51] which favors phonon transport at times beyond this coupling time, electrons may still move ballistically or diffuse some 100 nm before equilibrating with the phonon bath.[36,41] The average temperature of the particles rises by about 250 K for an applied fluence of 320 J m^{-2}.

At sufficient fluence (for example, 1600 J m^{-2}) the temperature on the front side of the irradiated microparticles is high enough to melt a part of the particle mass, which would then no longer contribute to powder scattering and is thus not included in the temperature evaluation. Only after heat diffusion and recrystallization will this energy be transported to the back side of the particle and detected as lattice expansion.

Fragmentation follows a thermoelastic driving mechanism, which is illustrated in Fig. 9. The SAXS region of the scattering from excited particles shows distinct signals that include small-angle scattering from nanoparticles in the 12–24 nm range at a delay of 100–200 ps, probably emitted from the front side during excess heating and melting of this surface part. At later delays and high fluence the SAXS signal is stationary with a slope of q^{-4}, but it does exhibit changing amplitude. This indicates that new particles are formed that exceed the 50 nm resolution limit of the experiment preventing their size to be resolved. However, the additional scattering is proportional to the change in surface area. Therefore, fragmentation of the microparticles progresses with increasing fluence and delay. Beyond about 1 ns, the scattering remains stationary, indicating the completion of the fragmentation process. The signal amplitude can be used to estimate the fragment size, which is found to be about 80 nm, if spherical fragments are assumed. We identify a fragmentation threshold of <750 J m^{-2}, at which the first signs of particle rupture appear, producing only a few fragments. This matches well with the absorbed-fluence value of 370 J m^{-2} reported by Spellauge *et al.*[24] For fluence values up to 2700 J m^{-2}, the number of fragments increases to 3400,

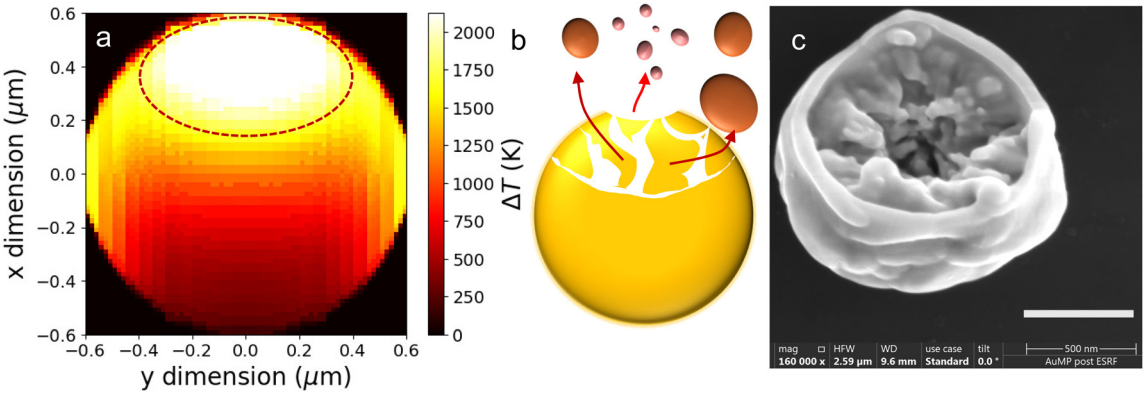

Fig. 9 (a) Temperature distribution at 1 ns of the simulated microparticle excitation at 717 J m^{-2} with the region of the highest temperature marked by a dashed line. (b) Sketch of the proposed mechanism with thermoelastic fracture of that part of the region at the highest temperature together with the generation of few-nm sized particles at the very front side after phase explosion. (c) Example of an SEM image of an irradiated microparticle with a central cavity that may be linked to thermoelastic fracture.

making this process very effective. The number of very small nanoparticles is still low (1–2.5%), while the number of produced nanoclusters is probably below the detection limit due to the dominance of the signal produced by the large fragmented particles. To increase the yield of these clusters, a higher fluence has to be applied, which will drive the overall particle temperature closer to evaporation and spinodal decomposition, thus causing phase explosion. The observed thermal kinetics, fragmentation time scale, and fragment sizes indicate a mixture of two mechanisms: stress-induced fragmentation, in which parts of the microparticles may remain in the solid state, and the forces arising from the temperature gradient between the front and back sides of the microparticles complemented by photothermal fragmentation at fluences well above the photomechanical fragmentation threshold.

Author contributions

This research program was conceived and designed by AP and SR. The samples were prepared by MT. The experiment was conducted by all authors. Analysis was performed by YP and AP. The manuscript was initially written by YP and AP with contributions from all authors.

Conflicts of interest

There are no conflicts to declare.

Data availability

The raw data will be made available after the expiration of the embargo (2027) at https://doi.org/10.15151/ESRF-ES-1560212245. Additionally, these data and reduction routines (Python scripts) are available upon request from anton.plech@kit.edu.

Also, we have posted a version of this manuscript on Arxiv arXiv:2510.02011.

Supplementary information (SI) is available. See DOI: https://doi.org/10.1039/d5nr04365d.

Acknowledgements

This work was supported by the German Science Foundation DFG under contract 491072288 and by the Helmholtz Programme “From Matter to Materials and life”. We acknowledge the European Synchrotron Radiation Facility (ESRF) for provision of synchrotron radiation facilities under proposal number SC5562 and we would like to thank M. Kozhaev for assistance and support in using beamline ID09. We would like to thank Maximilian Spellauge for useful discussions.

References

1 R. Streubel, G. Bendt and B. Gökce, *Nanotechnology*, 2016, **27**, 205602.
2 M. Tack, M. Usama, N. Kazamer, K. S. Exner, M. Brodmann, S. Barcikowski and S. Reichenberger, *ACS Appl. Energy Mater.*, 2024, **7**, 4057–4067.
3 D. Zhang, B. Gökce and S. Barcikowski, *Chem. Rev.*, 2017, **117**, 3990–4103.
4 A. Takami, H. Kurita and S. Koda, *J. Phys. Chem. B*, 1999, **103**, 1226–1232.
5 C. Chen and L. V. Zhigilei, *Appl. Phys. A*, 2023, **129**, 288.
6 A. Plech, J. Boneberg and P. Leiderer, *Laser Photonics Rev.*, 2009, **3**, 435.
7 Z. Swiatkowska-Warkocka, A. Pyatenko, K. Koga, K. Kawaguchi and H. W. N. Koshizaki, *J. Phys. Chem. C*, 2017, **121**, 8177–8187.
8 V. Amendola, D. Amans, Y. Ishikawa, N. Koshizaki, S. Scirè, G. Compagnini, S. Reichenberger and S. Barcikowski, *Chem. – Eur. J.*, 2020, **26**, 9206–9242.

9 S. Reich, J. Göttlicher, A. Ziefuss, R. Streubel, G. Smolentsev, A. Letzel, S. Barcikowski, A. Menzel, O. Mathon, S. Pascarelli, T. Baumbach and M. Zuber, *Nanoscale*, 2020, **12**, 14011–14020.
10 V. Amendola and M. Meneghetti, *Phys. Chem. Chem. Phys.*, 2009, **11**, 3805–3821.
11 S. Zerebecki, S. Reichenberger and S. Barcikowski, *J. Phys. Chem. A*, 2020, **124**, 11125–11132.
12 A. Letzel, M. Santoro, J. Frohleiks, A. R. Ziefuß, S. Reich, A. Plech, E. Fazio, F. Neri, S. Barcikowski and B. Gökce, *Appl. Surf. Sci.*, 2018, **473**, 828–837.
13 S. Reich, A. Letzel, B. Gökce, A. Menzel, S. Barcikowski and A. Plech, *ChemPhysChem*, 2019, **20**, 1036–1043.
14 Y. Ihm, D. H. Cho, D. Sung, D. Nam, C. Jung, T. Sato, S. Kim, J. Park, S. Kim, M. Gallagher-Jones, Y. Kim, R. Xu, S. Owada, J. H. Shim, K. Tono, M. Yabashi, T. Ishikawa, J. Miao, D. Y. Noh and C. Song, *Nat. Commun.*, 2019, **10**, 2411.
15 A. R. Ziefuss, S. Reich, S. Reichenberger, M. Levantino and A. Plech, *Phys. Chem. Chem. Phys.*, 2020, **22**, 4993–5001.
16 A. Plech, M. Tack, H. Huang, M. Arefev, A. R. Ziefuss, M. Levantino, H. Karadas, C. Chen, L. V. Zhigilei and S. Reichenberger, *ACS Nano*, 2024, **18**, 10527–10541.
17 J. Hwang, Y. Ihm, D. Nam, J. Shin, E. Park, S. Y. Lee, H. Lee, S.-P. Heo, S. Kim, J. Y. Ahn, J. H. Shim, M. Kim, I. Eom, D. Y. Noh and C. Song, *Sci. Adv.*, 2024, **10**, eadl6409.
18 P. Wagener and S. Barcikowski, *Appl. Phys. A*, 2010, **101**, 435–439.
19 O. Havelka, M. Cvek, M. Urbánek, D. Łukowiec, D. Jašíková, M. Kotek, M. Černík, V. Amendola and R. Torres-Mendieta, *Nanomaterials*, 2021, **11**, 1538.
20 M. Spellauge, M. Tack, R. Streubel, M. Miertz, K. S. Exner, S. Reichenberger, S. Barcikowski, H. P. Huber and A. R. Ziefuss, *Small*, 2023, **19**, 2206485.
21 T. Himeda, R. Kunitomi, R. Nabeya, T. Zako and T. Asahi, *Beilstein J. Nanotechnol.*, 2025, **16**, 1088–1096.
22 T. Fromme, R. Müller, L. Krenz, L. K. Tintrop, I. Sanjuán, T. C. Schmidt, K. M. Tibbetts, C. Andronescu, S. Reichenberger and S. Barcikowski, *J. Phys. Chem. C*, 2025, **129**, 2953–2965.
23 S. Siebeneicher, F. Waag, M. E. Castillo, V. V. Shvartsman, D. C. Lupascu and B. Gökce, *Nanomaterials*, 2020, **10**, 359.
24 M. Spellauge, R. Auer, M. Tack, F. Limani, D. Redka, A. R. Ziefuss, S. Barcikowski and H. P. Huber, *Arxiv*, 2025, DOI: 10.48550/arXiv.2512.13127.
25 G. Paltauf and H. Schmidt-Kloiber, *Appl. Phys. A*, 1997, **68**, 525–531.
26 P. G. Kuzmin, G. A. Shafeev, A. A. Serkov, N. A. Kirichenko and M. E. Shcherbina, *Appl. Surf. Sci.*, 2014, **294**, 15–19.
27 R. Sattari, C. Dieling, S. Barcikowski and B. Chichkov, *J. Laser Micro/Nanoeng.*, 2008, **3**, 100–105.
28 M. Levantino, Q. Kong, M. Cammarata, D. Khakhulin, F. Schotte, P. Anfinrud, V. Kabanova, H. Ihee, A. Plech, S. Bratos and M. Wulff, *C. R. Phys.*, 2021, **22**, 75–94.
29 A. Plech, S. Ibrahimkutty, S. Reich and G. Newby, *Nanoscale*, 2017, **9**, 17284–17292.
30 V. Kotaidis and A. Plech, *Appl. Phys. Lett.*, 2005, **87**, 213102.
31 V. Kotaidis, C. Dahmen, G. von Plessen, F. Springer and A. Plech, *J. Chem. Phys.*, 2006, **124**, 184702.
32 O. Spalla, S. Lyonnard and F. Testard, *J. Appl. Crystallogr.*, 2003, **36**, 338–347.
33 C. Schlumberger, C. Scherdel, M. Kriesten, P. Leicht, A. Keilbach, H. Ehmann, P. Kotnik, G. Reichenauer and M. Thommes, *Microporous Mesoporous Mater.*, 2022, **329**, 111554.
34 L. Alber, V. Scalera, V. Unikandanunni, D. Schick and S. Bonetti, *Comput. Phys. Commun.*, 2021, **265**, 107990.
35 J. Hohlfeld, S.-S. Wellershoff, J. Gudde, U. Conrad, V. Jahnke and E. Matthias, *Chem. Phys.*, 2000, **251**, 237–258.
36 A. Plech, P. Gaal, D. Schmidt, M. Levantino, M. Daniel, S. Stankov, G. Buth and M. Albrecht, *New J. Phys.*, 2024, **26**, 103024.
37 A. Pyatenko, H. Wang, N. Koshizaki and T. Tsuji, *Laser Photonics Rev.*, 2013, **7**, 596–604.
38 P. O'Keeffe, D. Catone, L. Di Mario, F. Toschi, M. Magnozzi, F. Bisio, A. Alabastri, R. Proietti Zaccaria, A. Toma, G. Della Valle and A. Paladini, *Laser Photonics Rev.*, 2021, **15**, 2100017.
39 P. Buffat and J.-P. Borel, *Phys. Rev. A*, 1976, **13**, 2287–2298.
40 P. Laven, *Appl. Opt.*, 2003, **42**, 436–444.
41 B. Rethfeld, K. Sokolowski-Tinten, D. von der Linde and S. I. Anisimov, *Phys. Rev. B:Condens. Matter Mater. Phys.*, 2002, **65**, 092103.
42 M. Z. Mo, Z. Chen, R. K. Li, M. Dunning, B. B. L. Witte, J. K. Baldwin, L. B. Fletcher, J. B. Kim, A. Ng, R. Redmer, A. H. Reid, P. Shekhar, X. Z. Shen, M. Shen, K. Sokolowski-Tinten, Y. Y. Tsui, Y. Q. Wang, Q. Zheng, X. J. Wang and S. H. Glenzer, *Science*, 2018, **360**, 1451–1455.
43 A. Plech, V. Kotaidis, S. Grésillon, C. Dahmen and G. von Plessen, *Phys. Rev. B:Condens. Matter Mater. Phys.*, 2004, **70**, 195423.
44 H. Huang and L. V. Zhigilei, *Sci. China:Phys., Mech. Astron.*, 2022, **65**, 274206.
45 C.-Y. Shih, R. Streubel, J. Heberle, A. Letzel, M. V. Shugaev, C. Wu, M. Schmidt, B. Gökce, S. Barcikowski and L. V. Zhigilei, *Nanoscale*, 2018, **10**, 6900–6910.
46 H. Sakurai, K. Konishi, H. Tamaru, J. Yumoto and M. Kuwata-Gonokami, *Commun. Mater.*, 2021, **2**, 38.
47 M. Spellauge, C. Doñate-Buendía, S. Barcikowski, B. Gökce and H. P. Huber, *Light: Sci. Appl.*, 2022, **11**, 31–43.
48 M. Cammarata, M. Lorenc, T. K. Kim, J. H. Lee, Q. Y. Kong, E. Pontecorvo, M. L. Russo, G. Schiró, A. Cupane, M. Wulff and H. Ihee, *J. Chem. Phys.*, 2006, **124**, 124504.
49 K. Boboridis, G. Pottlacher and H. Jäger, *Int. J. Thermophys.*, 1999, **20**, 1289–1297.
50 D. R. Lide, *CRC Handbook of Chemistry and Physics*, CRC Press, Boca Raton, FL, 95th edn, 2015.
51 B. Guzelturk, J. K. Utterback, I. Coropceanu, V. Kamysbaev, E. M. Janke, M. Zajac, N. Yazdani, B. L. Cotts, S. Park, A. Sood, M.-F. Lin, A. H. Reid, M. E. Kozina, X. Shen, S. P. Weathersby, V. Wood, A. Salleo, X. Wang, D. V. Talapin, N. S. Ginsberg and A. M. Lindenberg, *ACS Nano*, 2020, **14**, 4792–4804.